Computation & theory

B$_2$O and B$_4$N monolayers supported single-metal atom as highly efficient bifunctional electrocatalyst for OER and ORR

Feng Gao[1], Yuhua Wei[1], Jiguang Du[2,*] (iD), and Gang Jiang[1,*]

[1] *Institute of Atomic and Molecular Physics, Sichuan University, Chengdu 610065, China*
[2] *College of Physics, Sichuan University, Chengdu 610065, China*

ABSTRACT

The development of high efficiency, stable and economical electrocatalysts is an ideal choice for water electrolysis, fuel cells and metal air cells, and an important innovation in the future energy field. Bifunctional or even multifunctional catalysts have higher performance and lower cost than monofunctional catalysts, which is currently an emerging focus in the development of electrocatalysts. The single-atom catalysts (SACs) of two-dimensional (2D) materials-supported transition metal (TM) atoms have attracted great attention because of their ability to make full use of metal atoms and remarkable catalytic performance. In this work, the oxygen evolution reaction (OER) and oxygen reduction reaction (ORR) catalytic properties of B$_4$N and B$_2$O monolayers supported TM atoms have been systematically evaluated based on first-principles calculations. The adsorption free energy of key intermediates (OOH*, O* and OH*) on the catalyst determines the catalytic activity toward OER and ORR. The calculation results exhibit that Ni@B$_4$N and Pd@B$_2$O systems are potential bifunctional electrocatalysts with the overpotential (η) of OER/ORR being just 0.45/0.43 V and 0.56/0.47 V, respectively, which are comparable to the known noble metal catalysts. Therefore, the study of catalytic activity of SACs on 2D substrate materials provides a broad prospect for the development of stable, low-cost, high-activity noble metal-free electrocatalysts, and provides help for solving energy and environmental problems.

Introduction

Currently, with the human demand for energy bigger and bigger, the traditional fossil energy cannot meet the demand of human society in the future energy [1, 2]. Therefore, water electrolysis [3, 4], metal air batteries [5, 6], fuel cells [7–9] and other sustainable energy production technologies are increasingly being people's attention. The electrocatalysts oxygen evolution reaction (OER) and oxygen reduction reaction (ORR) are the two key reaction of the current advanced energy conversion technology [10, 11]. It is well known that both reactions kinetics rate is slow, which limits the development of related energy conversion and storage technology [12]. So far, usual choice is given priority with noble metal or noble metal oxide catalysts to accelerate the reaction rate of OER and ORR. Among them, the most widely used catalysts are Pt for ORR and Ru or Ir oxides for OER [13–16]. However, the high prices and scarcity of these noble metals restrict their large-scale and wider industrial applications. Hence, development of low-cost and high catalytic activity noble metal-free catalysts has very important practical significance and urgency [5]. Previous research has shown that carbon-based materials, transition metal hydroxides, transition metal sulfides and composites composed of these materials all have good catalytic activity [17–20].

The deposition of transition metal (TM) atoms on the surface of materials to form single-atom catalysts (SACs) is a new frontier in catalytic research, which opens a new door for us to reveal the catalytic process on atomic scale [21–25]. In the past few years, a growing number of reports indicated that SACs can be widely used for CO oxidation [26, 27], fuel cells [5] and water splitting. SACs can ensure maximum atomic utilization and form more adjustable active sites. However, as the metal particle size reduces to a single atom, the increase in the surface free energy is likely to lead to metal aggregation [24]. Consequently, to keep SACs excellent catalytic performance, choosing reasonable metal atoms and selecting the appropriate substrate materials are very crucial to stabilize the isolated metal atom. In recent years, catalysts based on two-dimension (2D) materials have attracted widespread attention due to their high activity and a large number of reaction sites [28–35]. 2D materials as SACs substrate have been

extensively studied, which has opened up a new frontier field for the search of efficient catalysts [36–41]. More importantly, 2D catalysts are potential bifunctional catalysts with both OER and ORR activities. For energy conversion technologies, bifunctional catalysts have higher catalytic performance than two single functional catalysts [42, 43]. In addition, compared with two separate single functional catalysts, bifunctional catalysts can reduce product costs due to less equipment usage and simpler production process.

The catalytic activity of single atom and substrate combinations requires a simple and efficient descriptor for design estimation [42, 44–46]. Nevertheless, a complete description of how SACs and their coordination environment affect OER and ORR activity remains unclear. In this regard, there is an urgent need to fully understand the catalytic activity trends of different single atom and substrate combinations, which can help guide the direction of adjusting the performance of SACs. Recently, B_4N and B_2O monolayers materials have been successfully predicted using first-principles calculation methods [47, 48], and a large number of theoretical studies have been carried out to study their applications as cathode materials for batteries and catalysts for hydrogen evolution reactions (HER) [49–53]. All previous studies indicated that B_4N and B_2O monolayers were two promising SACs substrates [47, 48]. Based on this, using 2D B_2O and B_4N as substrate materials, this paper utilizes density functional theory (DFT) to study the OER and ORR catalytic activities of TM atoms supporting on its surface, and to explore the mechanism of OER and ORR. We have studied the 3d and 4d group TM atoms, including Sc, Ti, V, Cr, Mn, Fe, Co, Ni, Zn, Cu and Pd. The scale relationship between the Gibbs free energy (ΔG) of OER and ORR intermediate adsorption is used to describe the trend of catalytic activity. It is found that the d band center (ε_d) of the doped TM atoms is strongly correlated with the catalytic activity of OER and ORR. Finally, our calculated results suggest that Ni@B_4N and Pd@B_2O systems could be used as bifunctional electrocatalysts with excellent performance, and the overpotentials (η) of ORR and OER are even as low as 0.43/045 V and 0.47/0.56 V, respectively. The effect of single TM atom doping on ORR and OER catalytic activity of 2D materials is further investigated. Our study not only provides electrochemists with a promising bifunctional SACs

for ORR and OER, which may stimulate the electrochemists to synthesize it experimentally, but also provides theoretical basis and more opportunities for the design of efficient bifunctional catalysts.

Computational methods

All the calculations in the present study were carried out on spin-polarized DFT using the Vienna ab initio simulation package (VASP) code [54, 55]. The projector augmented wave (PAW) pseudopotentials were used to treat the core electrons [56]. The Perdew–Burke–Ernzerhof (PBE) [57] functional of the generalized gradient approximation (GGA) [58] was used to describe the electronic exchange and correlation interactions. A cutoff energy was set as 500 eV for the plane-wave basis set, and the convergence criteria for energy and force were less than 10^{-5} eV and 10^{-2} eV/Å, respectively. Moreover, van der Waals (vdW) corrections were considered by using the dispersion correction of DFT-D3 method of Grimme [59, 60]. A vacuum distance was not less than 15 Å to avoid the interlayer interaction in the z-direction. The Brillouin zones were sampled with $3 \times 3 \times 1$ Monkhorst–Pack meshes for B_2O monolayer and $5 \times 5 \times 1$ for B_4N monolayer, respectively. The dynamic stability of B_4N and B_2O monolayers was verified by using the PHONOPY code [61] implemented in VASP using the density functional perturbation theory (DFPT) [62]. A more precise k-mesh of $7 \times 7 \times 1$ and $3 \times 3 \times 1$ was used for electronic structure calculations and ab initio molecular dynamics (AIMD), respectively. In AIMD simulations, integration of the equations of motion proceeds with time steps of 2.0 fs for different temperature ranges. Typical simulations ran for 3000 steps with the time scale about 6 ps. The isokinetic ensemble (NVT) was employed for the ions, where the ion temperature T_i was fixed using velocity scaling. For more computational details, please see the Supporting Information.

Results and discussion

As shown in Fig. 1a, for the atomic structure of 2D B_2O, there are two B and one O atoms in a primitive unit, and this structure has the space group Cmmm (No. 65). The optimized B-B (1.709 Å), B-O (1.338 Å) bond lengths, the B-B-B angle (107.5°) and lattice parameters (a = b = 3.937 Å) obtained from our calculations are in accordance with the previous work [48, 51, 53]. For the 2D B_4N atomic structure, the structure reveals Cmmm symmetry with orthogonal lattices. The optimized structural parameters are a = 2.97 Å, b = 10.70 Å, and B-N bond length is 1.334 Å (see Fig. 1b). These calculation results are consistent with the previous report [47, 50]. To evaluate the dynamic stability of B_2O and B_4N monolayers, we calculated their phonon spectra, as shown in Fig. 1c. The absence of negative frequencies confirmed the dynamic stability of B_2O and B_4N monolayers. The highest frequency of B_2O and B_4N monolayers is about 50 THz, indicating that $B - O$, $B - B$ and $B - N$ in B_2O and B_4N monolayers have strong interactions. The thermal stability of B_2O and B_4N monolayers was simulated by AIMD. Figure 1d shows that the mean value of the total potential energy during the AIMD simulation oscillates within a narrow range, and the overall configuration of B_2O and B_4N monolayers remains good after 6 ps AIMD simulation, which confirms their thermal stability. Then, the structural optimization of B_2O and B_4N monolayers is performed based on a $4 \times 4 \times 1$ and $2 \times 2 \times 1$ supercell.

To explore the catalytic performance of the B_2O and B_4N monolayers, we study the active sites on the surface. According to the symmetry of the structure, there are three possible sites of TM atoms adsorbed on the monolayers of B_2O and B_4N. These possible sites are marked as top (T), bridge (B) and center sites, respectively, as shown in Fig. S2(a-b). The stability of TM atoms doping on B_2O and B_4N monolayers by analyzing the binding energy (E_b), thus finding the optimal active site. Finally, it can be found from Table S1 that after geometry optimization, only the center site of the hexagon has the lowest E_b, while the other sites have higher E_b. In addition, existing studies have shown that atomic defects are regarded as the active site of catalysis [53, 63], and both the B_2O and B_4N monolayers have the advantage of natural defect structure, so we finally select the defect center site to stabilize solid TM atoms, as shown in Fig. 2a and c. Irreversible detachment of the central transition metal atom from the catalyst significantly limits catalyst durability. To investigate the stability of TM@B_4N and TM@B_2O systems, we calculated their E_b of TM atoms supporting on the center site. The calculated E_b are shown in Fig. 2b and d, where all

● B ● N ● O
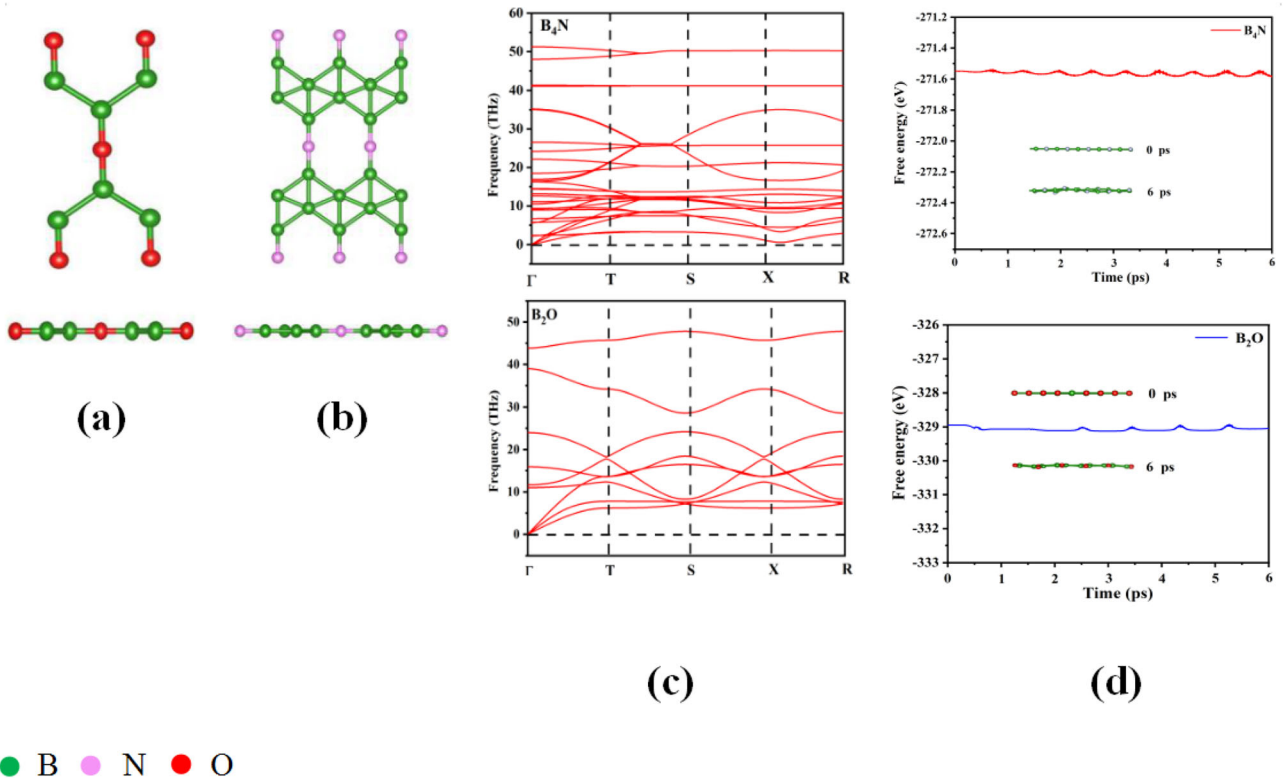
Figure 1 The top and side views of the optimized primitive cell **a** B₂O **b** B₄N. **c** Phonon band structure of the 2D B₂O and B₄N. **d** The fluctuation of total energy during AIMD simulations at 300 K. The insets show the structures of the B₂O and B₄N monolayers at 0 and 6 ps, respectively.

● B ● N ● O ● TM=Sc, Ti, V, Cr, Mn, Fe, Co, Ni, Pd
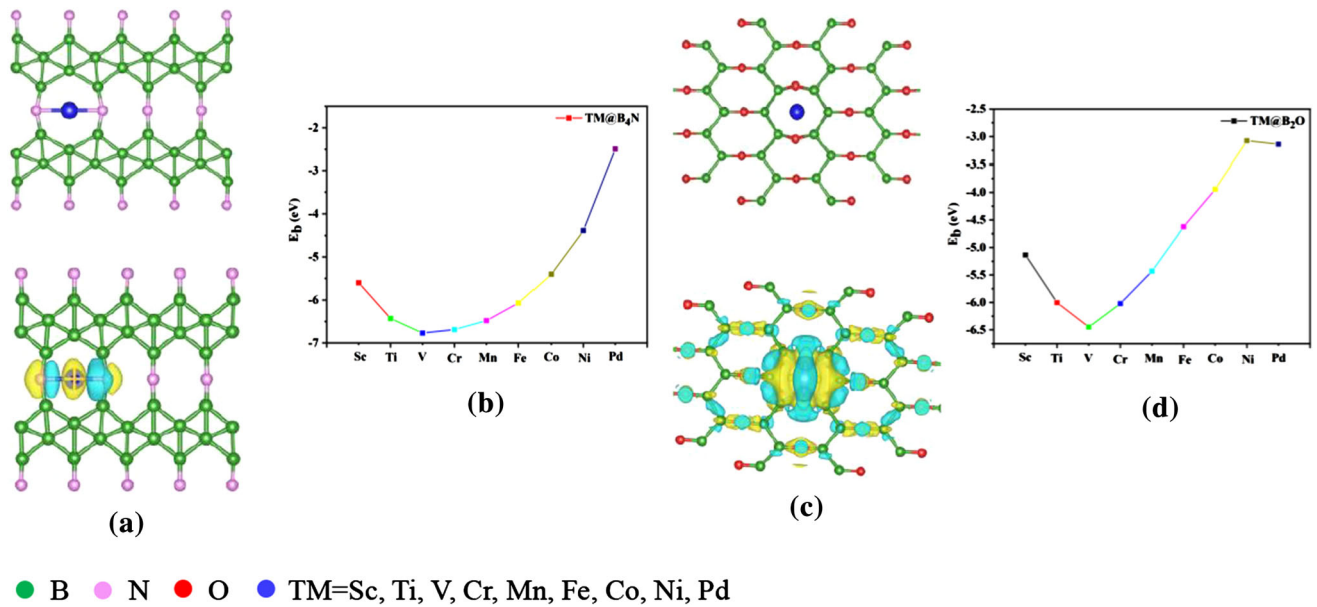
Figure 2 a The top view of the optimal TM adsorption site on B₄N monolayer and corresponding charge density difference profiles. **b** The E_b of TM@B₄N systems. **c** The top view of the optimal TM adsorption site on B₂O monolayer and corresponding charge density difference profiles. **d** The E_b of TM@B₂O systems.

negative values of E_b indicate that the B_4N and B_2O monolayers stabilize these doped TM atoms against clustering. This may be because the boron atom forms a very strong coordination bond when it provides 2p electron pairs to the vacant d orbital of the TM atoms. In order to better understand the interaction between TM atoms and B_4N and B_2O monolayers, we also plot the charge density difference distribution. In both cases, it has been observed that the center TM atoms are exposed and depleted to the B_2O and B_4N monolayers, with the yellow and cyan surfaces showing electron accumulation and loss,

respectively. The bonding between TM atoms and O or N atoms is more stable than that between TM atoms and B atom so that TM atoms are bound around O and N atoms, thus residing at the center site and reducing the aggregation between TM atoms. These results indicate that there is a strong interaction between TM atoms and B_4N and B_2O monolayers, and the structure is stable after doping TM atoms.

Different TM atoms anchoring on B_4N and B_2O monolayers have different electronic structures, which provides a new method for understanding

Figure 3 Calculated the partial density of states (PDOS) of the TM@B_4N systems. The Fermi level is set at zero (pink dashed line) and the d band center (ε_d) and are marked by cyan dashed line.
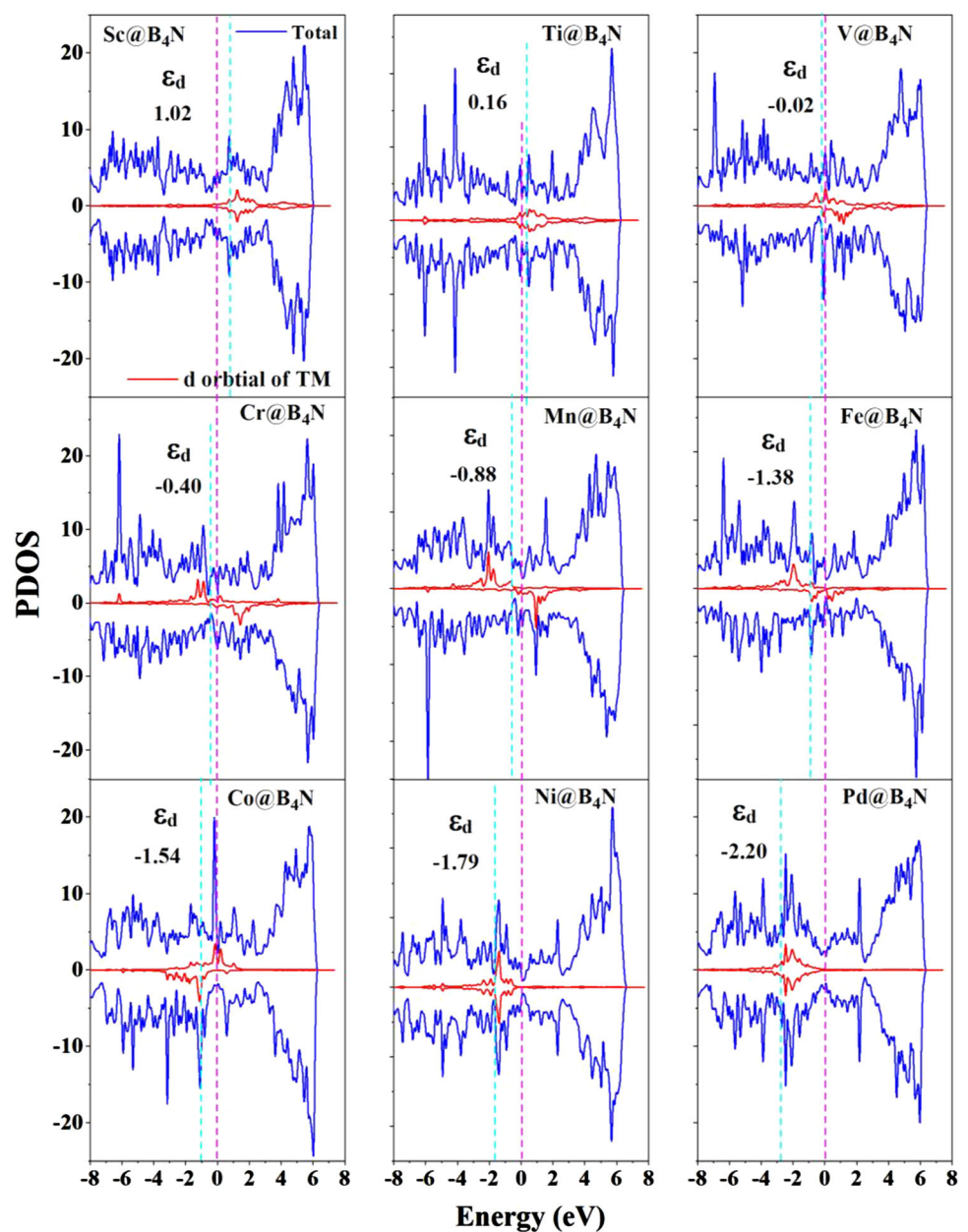
Figure 4 Calculated the partial density of states (PDOS) of the TM@B$_2$O systems. The Fermi level is set at zero (pink dashed line) and the d band center (ε_d) and are marked by cyan dashed line.
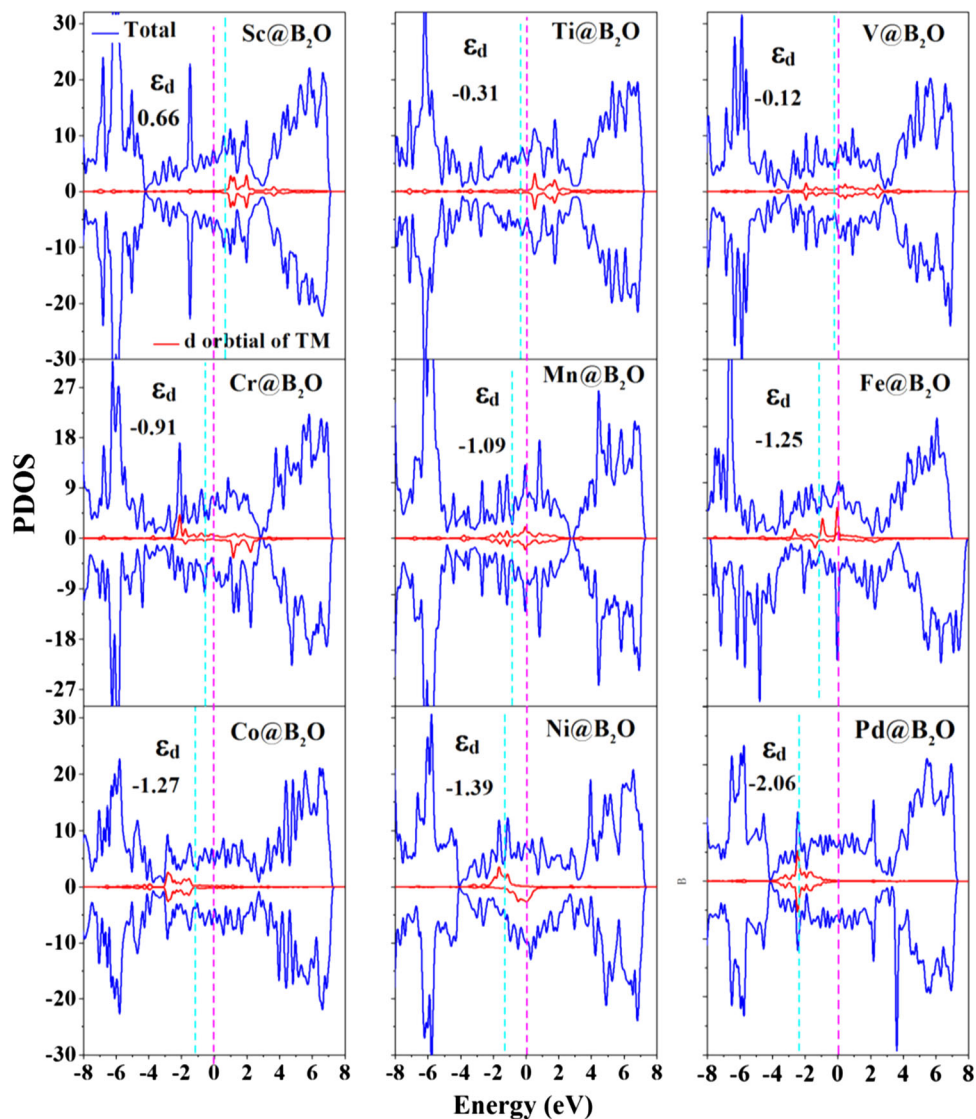

their catalytic properties. We calculate the values of the densities of states of partial wave (PDOS) for d orbitals of different TM atoms anchored on the B$_4$N and B$_2$O monolayers, as shown in Figs. 3 and 4. All the TM@B$_4$N and TM@B$_2$O systems considered in this work exhibit metallic properties, indicating that all structures have good electrical conductivity. It is well known that the ε_d is used to analyze the descriptor of the strength of the interaction between adsorbates and substrates [64–67]. The large number of d electrons in TM atoms and low ε_d energy levels usually result in weaker interactions with OH *, O* and OOH* adsorbates [68]. This is because the interaction between TM atoms and the adsorbates occurs through their electron level hybridization and charge transfer from TM atoms to the adsorbates. The

PDOS in the figure displays that as the number of d electrons in TM atoms increases, we can see the ε_d shift towards the lower energy relative to the Fermi level. The results indicate that the interaction strength of adsorbates on B$_4$N and B$_2$O monolayers presents the following trend: Sc > Ti > V > Cr > Mn > Fe > Co > Ni > Pd. Nørskov et al. believed that the interaction intensity of adsorption intermediates on the catalyst was too strong, and the active center of the catalyst would be poisoned [69]. However, if the interaction is too weak, it is difficult to activate the reactants or intermediates and initiate the catalytic process. Therefore, it is a challenge to identify promising materials with suitable adsorption energies of the reaction intermediates. In order to verify the above conclusions, the ΔG of OER and ORR

reaction intermediates corresponding to the ε_d of TM@B_4N and TM@B_2O systems is calculated based on Eqs. (S23)-(S25), as shown in Fig. S3. One can find from Fig. S3 that there are good relationships between the ε_d and ΔG_{O*}, ΔG_{OH*} as well as ΔG_{OOH*}. We can conclude that for TM atoms in the same row of the periodic table, an increase in the number of d electrons tends to weaken the adsorption free energy of adsorbates. Therefore, these results exhibit the negative correlation between the ε_d and ΔG_{O*}, ΔG_{OH*} and ΔG_{OOH*}. Considering the adsorption properties of intermediates can determine the reaction activity, such linear relationship can help to design catalysts more efficiently. This phenomenon has also been observed in experiments [70] and other theoretical studies [42, 71]. Therefore, we can adjust the interaction strength to the optimal values of OER and ORR performance by changing the doped TM atoms. As shown above, the ΔG of the adsorbed states (OH*, O* and OOH*) on the catalyst determine the rate-determining steps and catalytic activity of OER and ORR. For the ideal catalyst, the total formation energy of ORR is 4.92 eV, and the ideal adsorption values of ΔG_{OH*}, ΔG_{O*} and ΔG_{OOH*} are 1.23, 2.46 and 3.69 eV, respectively, and the energy distance between the two adjacent intermediate states is 1.23 eV (when U = 0 V). Therefore, OER and ORR reaction can occur at the thermodynamic limit, where the corresponding η value is zero. However, in reality, the energy distance between adjacent intermediate states is difficult to satisfy the condition of equality, resulting in limited reaction. The η^{OER} is determined by the maximum energy distance between two adjacent intermediate states, while the η^{ORR} is determined by the minimum energy distance between two adjacent intermediate states. We calculate the η^{OER} and η^{ORR} of all TM@B_4N and TM@B_2O systems as shown in Fig. 5. Our results demonstrate that the stable position of the intermediate on the catalyst is at the top of the TM atoms, and only Ni@B_4N and Pd@B_2O system has good catalytic activity of ORR and OER, which are two potential bifunctional catalysts. The η^{OER} of Ni@B_4N system is 0.45 V, comparable to the calculated RuO_2 catalyst (0.42 V) [72]. The η^{ORR} of Pd@B_2O system (0.56 V) is slightly higher than that of conventional RuO_2 catalyst. The best catalyst for ORR is Ni@B_4N system with the lowest η^{ORR} value of 0.43 V, followed by Pd@B_2O system (0.47 V). It is worth noting that their η^{ORR} values are both lower than the reported value of the best catalyst Pt (0.48 V) [73].

The relationship among the Gibbs free energy ΔG_{OH*}, ΔG_{O*} and ΔG_{OOH*} of the intermediate can be used to analyze the OER and ORR trends of the catalyst. The scaling relationships of ΔG_{OH*} and ΔG_{OOH*}, ΔG_{OH*} and ΔG_{O*} in Ni@B_4N and Pd@B_2O systems are shown in Fig. 6. Obviously, for the Ni@B_4N system, ΔG_{OOH*} can be expressed as a function of ΔG_{OH*} by the equation: $\Delta G_{OOH*} = 0.67\Delta G_{OH*} + 2.75$. The relationship between ΔG_{OOH*} and ΔG_{OH*} has a very high coefficient of certainty ($R^2 = 0.94$), indicating a strong linear relationship. Similarly, for Pd@B_2O system, there is a strong linear relationship between ΔG_{OOH*} and ΔG_{OH*}, which is expressed by the equation:
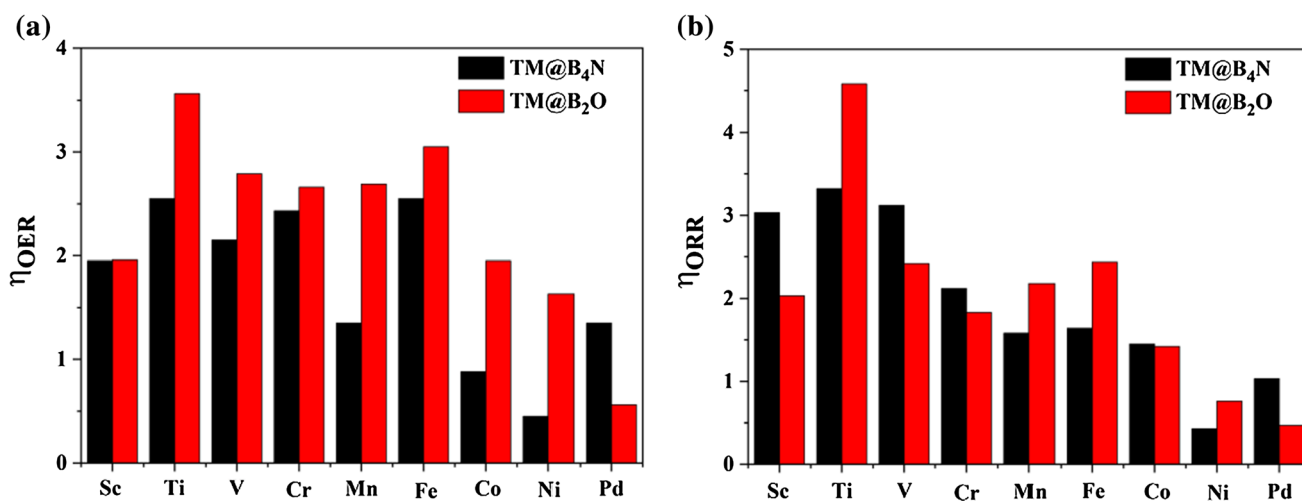

Figure 5 Summary of overpotentials of TM@B_4N and TM@B_2O systems for **a** OER and **b** ORR.

(a)

(b)
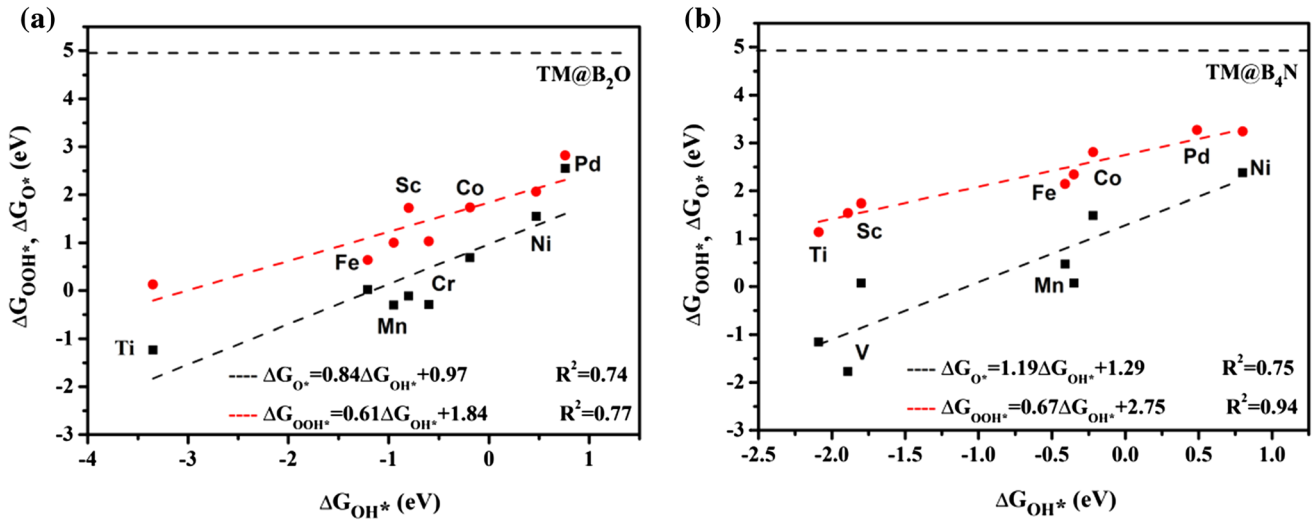
Figure 6 Scaling relationships between the adsorption free energies of adsorbates of **a** TM@B$_2$O and **b** TM@B$_4$N systems. The dashed horizontal line shows the O$_2$ initial state at 4.92 eV.

$\Delta G_{OOH*} = 0.61\Delta G_{OH*} + 1.84$, and has a high determination coefficient ($R^2 = 0.77$). The slope and constant separation in the relation between ΔG_{OOH*} and ΔG_{OH*} indicate that the intermediate OOH* and OH* form a single bond between oxygen and TM atoms. Then, through linear fitting, we can obtain the scaling relationship of ΔG_{OH*} and ΔG_{O*} for Ni@B$_4$N system: $\Delta G_{O*} = 1.19\Delta G_{OH*} + 1.29$, and the R^2 is 0.75. For the Pd@B$_2$O system, the scaling relationship is $\Delta G_{O*} = 0.94\Delta G_{OH*} + 0.97$ with the corresponding R^2 of 0.74. Note that the linear relationship between the ΔG_{OH*} and ΔG_{O*} is not as good as that of ΔG_{OH*} and ΔG_{OOH*} due to the different single metal–oxygen

bond nature of the OH* and O*. Different oxidation states have different contributions to the binding strength of oxygen atom and TM atoms, which more or less leads to the deviation from the linear scaling between them. As stated in Eq. (S17) and (S22), the η^{OER} and η^{ORR} are two function of four variables (ΔG_1, ΔG_2, ΔG_3 and ΔG_4). According to the scaling relationship of $\Delta G_1 + \Delta G_2 + \Delta G_3 + \Delta G_4 = 4.92$ eV, the η^{OER} and η^{ORR} can be reduced to two descriptors. On the grounds of the definitions of Eqs. (S13-S16) and (S18-S21), the two descriptors ΔG_{OH*} and ΔG_{O*}—ΔG_{OH*} are sufficient to describe the catalytic performance of OER and ORR. For the TM@B$_4$N and

(a)

(b)
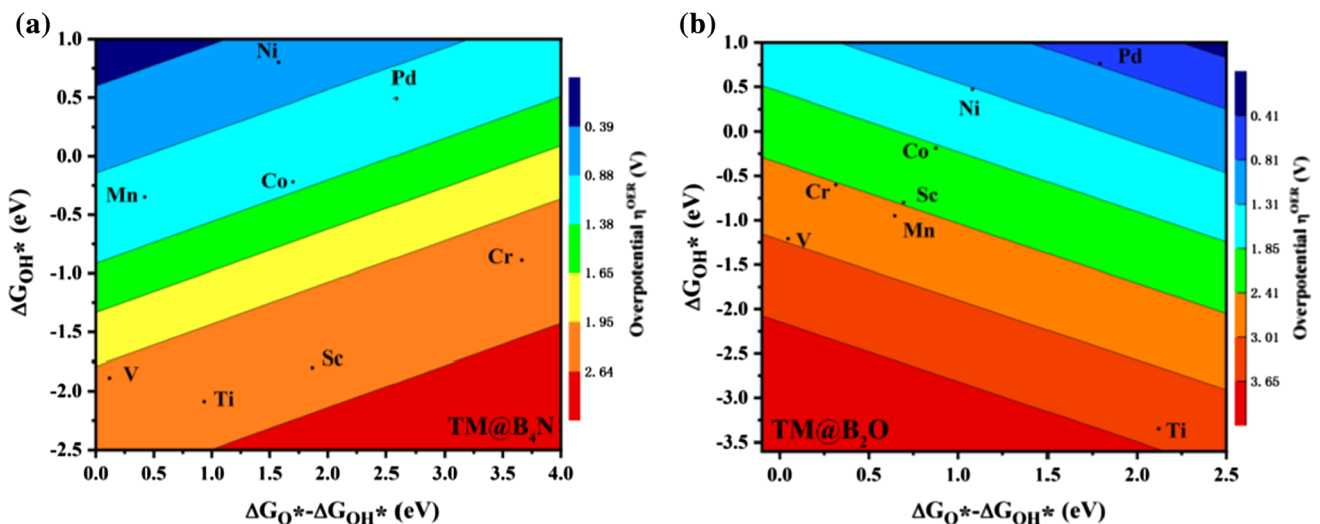
Figure 7 Colored contour plots of OER activity volcanoes for **a** TM@B$_4$N and **b** TM@B$_2$O systems showing the η^{OER} as a function of adsorption Gibbs free energies of the intermediates. The color bar represents the value of η.
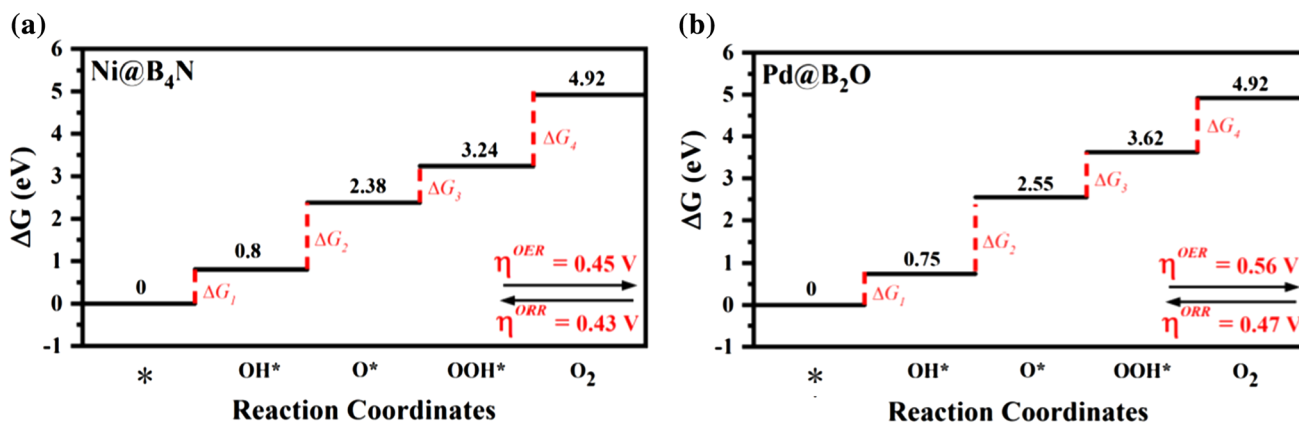
Figure 8 Gibbs free energy diagrams during the OER and ORR reaction pathways of **a** Ni@B$_4$N and **b** Pd@B$_2$O systems at 0 V versus standard hydrogen electrode.
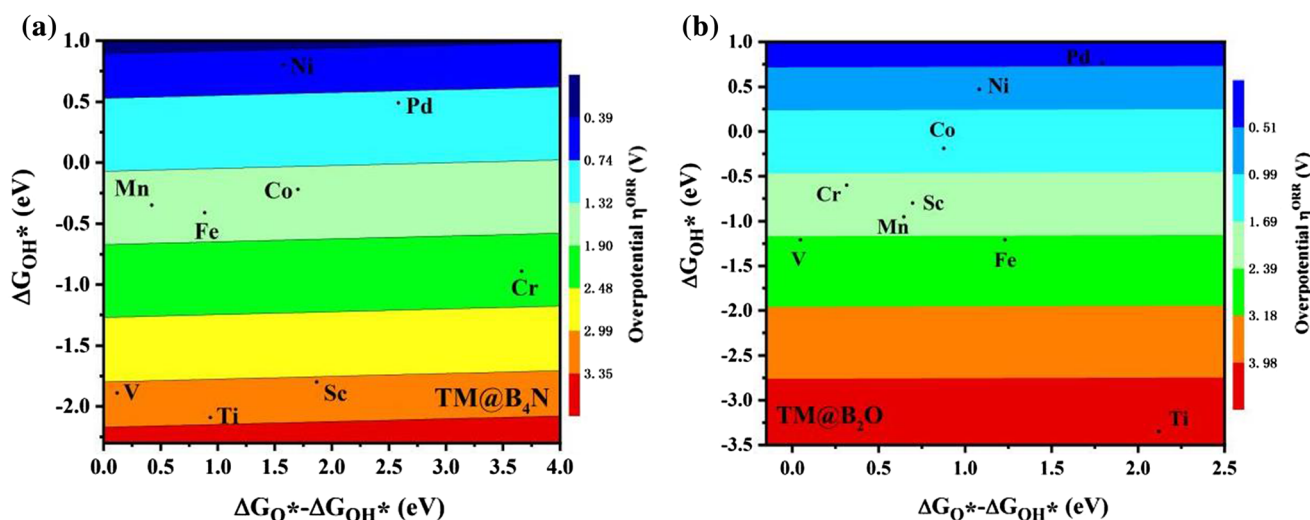
Figure 9 Colored contour plots of ORR activity volcanoes for **a** TM@B$_4$N and **b** TM@B$_2$O systems showing the η^{ORR} as a function of adsorption Gibbs free energies of the intermediates. The color bar represents the value of η.

TM@B$_2$O systems, we drew 2D volcano maps. As seen from Fig. 7, it can be found that under the optimum condition ($\Delta G_1 = \Delta G_2 = \Delta G_3 = 1.34$ eV), limiting η^{OER} of TM@B$_4$N and TM@B$_2$O systems are as low as 0.39 and 0.41 V, respectively. The blue region of the 2D volcano map shows the highest active area. Among the systems considered, Ni@B$_4$N and Pd@B$_2$O systems are potential catalysts, with η^{OER} of 0.45 and 0.56 V, respectively. As shown in Fig. 8, for the Ni@B$_4$N system, the fourth step (desorption of O$_2$) are the rate-determining steps, while the second step (O* formation) is the rate-determining step for the Pd@B$_2$O system. Figure 9 shows the trend of activity of ORR for TM@B$_4$N and TM@B$_2$O systems by using η^{ORR} as a function of the independent descriptors of ΔG_{OH*} and ΔG_{O*}—ΔG_{OH*}. Under

the optimal conditions ($\Delta G_1 = \Delta G_4 = -0.91$ eV), the theoretical η^{ORR} is as low as 0.39 V. The first step in the ORR pathway is that O$_2$ molecule is hydrogenated to OOH* through coupled proton electron transfer. Then OOH* is attacked by an additional proton electron pair to form O* atom and H$_2$O molecule. O* is then further hydrogenated to OH* before the second H$_2$O molecule formed. The most suitable catalysts for ORR are Ni@B$_4$N and Pd@B$_2$O systems. The η^{ORR} of Ni@B$_4$N system is found to be below 0.43 V, and the rate-determining step is to release of adsorbed OH*, while the release of adsorbed OH* is the rate-determining step for the Pd@B$_2$O system ($\eta^{ORR} = 0.47$ V) (see Fig. 8). Obviously, Ni@B$_4$N and Pd@B$_2$O systems, as potential efficient bifunctional catalysts for OER and ORR, can catalyze

both OER and ORR at the same active site. Calculated intermediates of ΔG_{OH*}, ΔG_{OH*} and ΔG_{OOH*} for the other systems are summarized in Fig. S4 and Table S2-S3. For the other systems, the formation of O* and OOH* in the second and third steps is the most difficult because it shows the maximum energy range and therefore becomes the most likely rate-determining step. The corresponding η^{OER} of these systems is too high to effectively catalyze OER. As OER electrocatalysts in practical application, they not only need more energy input, but also cause the lag of kinetic rate. In addition, due to the large required energy and slow reaction kinetics, it is difficult to remove the reaction intermediate products, thus leading to the active center deactivation and making the catalyst poison. Our results reveal that Ni@B$_4$N and Pd@B$_2$O systems are highly efficient and stable OER/ORR bifunctional catalysts and provide useful guidance for screening metal active centers of SACs on 2D materials.

Conclusions

In summary, we have systematically studied the stability and catalytic behavior of TM atoms doped at the center defect site on B$_2$O and B$_4$N monolayers based on the DFT method, aiming to search for potential bifunctional SACs for OER/ORR with high activity and stability. The results show that the adsorption strength of the intermediates on the active center of TM atoms is closely related to the ε_d. As the number of d electrons of doped TM atoms on the defect B$_2$O and B$_4$N monolayers increases, the ε_d moves to the lower energy level, which weakens the interaction between the intermediate and the active center of TM atoms. Therefore, the ideal OER and ORR catalysts can be selected by adjusting the doped TM elements. According to the volcanic maps of OER and ORR, it is found that Ni@B$_4$N system ($\eta^{OER} = 0.45$ V, $\eta^{ORR} = 0.43$ V) and Pd@B$_2$O system ($\eta^{OER} = 0.56$ V, $\eta^{OER} = 0.47$ V) as ORR/OER bifunctional SACs have a high application prospect, and their catalytic performance can be comparable to that of traditional noble metal-based catalysts. Considering the tons of structural candidates for such 2D substrates as well as the simple and tunable strain-engineering strategy, we wish the present theoretical basis will spur more interests and efforts in designing efficient bifunctional SACs in overall water splitting from both the theory and experiments.

Availability of data and material

All data generated or analyzed during this study are included in this published article and its supplementary information files.

Declarations

References

[1] Panwar NL, Kaushik SC, Kothari S (2011) Role of renewable energy sources in environmental protection: a review. Renew Sust Energ Rev 15:1513–1524

[2] Kolar JL (2000) Alternative energy technologies. Environ Qual Manage 10:45–54

[3] Jamesh M-I, Sun X (2018) Recent progress on earth abundant electrocatalysts for oxygen evolution reaction (OER) in alkaline medium to achieve efficient water splitting-a review. J Power Sources 400:31–68

[4] Li H, Wu Y, Li L, Gong Y, Niu L, Liu X, Wang T, Sun C, Li C (2018) Adjustable photocatalytic ability of monolayer g-C$_3$N$_4$ utilizing single-metal atom: density functional theory. Appl Surf Sci 457:735–744

[5] Huang Z-F, Wang J, Peng Y, Jung C-Y, Fisher A, Wang X (2017) Design of efficient bifunctional oxygen reduction/ evolution electrocatalyst: recent advances and perspectives. Adv Energy Mater 7:1700544

[6] Wang M, Qian T, Liu S, Zhou J, Yan C (2017) Unprecedented activity of bifunctional electrocatalyst for high power density aqueous zinc-air batteries. ACS Appl Mater Inter 9:21216–21224

[7] Jiao Y, Zheng Y, Jaroniec M (2015) Design of electrocatalysts for oxygen and hydrogen-involving energy conversion reactions. Chem Soc Rev 46:2060–2086

[8] Morales-Guio CG, Stern LA, Hu X (2014) Nanostructured hydrotreating catalysts for electrochemical hydrogen evolution. Chem Soc Rev 43:6555–6569

[9] Liu GS, You SJ, Tan Y, Ren NQ (2017) In situ photochemical activation of sulfate for enhanced degradation of organic pollutants in water. Environ Sci Technol 51:2339–2346

[10] Nguyen TV, White RE (1993) A water and heat management model for proton exchange-membrane fuel cells. J Electrochem Soc 140:2178–2186

[11] Liu H, Logan BE (2004) Electricity generation using an air-cathode single chamber microbial fuel cell in the presence and absence of a proton exchange membrane. Environ Sci Technol 38:4040–4046

[12] Rana M, Mondal S, Sahoo L, Chatterjee K, Karthik PE, Gautam UK (2018) Emerging materials in heterogeneous electrocatalysis involving oxygen for energy harvesting. ACS Appl Mater Inter 10:33737–33767

[13] Suen NT, Hung S-F, Quan Q, Zhang N, Xu Y-J, Chen HM (2017) Electrocatalysis for the oxygen evolution reaction: recent development and future perspectives. Chem Soc Rev 46:337–365

[14] Sealy C (2008) The problem with platinum. Mater Today 11:65–68

[15] Rossmeisl J, Qu ZW, Zhu H, Kroes GJ, Nørskov JK (2007) Electrolysis of water on oxide surfaces. J Electroanal Chem 607:83–89

[16] Reier T, Oezaslan M, Strasser P (2012) Electrocatalytic oxygen evolution reaction (OER) on Ru, Ir, and Pt catalysts: a comparative study of nanoparticles and bulk materials. ACS Catal 2:1765–1772

[17] Osgood H, Devaguptapu SV, Xu H, Cho J, Wu G (2016) Transition metal (Fe Co, Ni, and Mn) oxides for oxygen reduction and evolution bifunctional catalysts in alkaline media. Nano Today 11:601–625

[18] Qu K, Zheng Y, Dai S, Qiao SZ (2016) Graphene oxide-polydopamine derived N, S-codoped carbon nanosheets as superior bifunctional electrocatalysts for oxygen reduction and evolution. Nano Energy 19:373–381

[19] Qian L, Lu Z, Xu T, Wu X, Tian Y, Li Y, Huo Z, Sun X, Duan X (2015) Trinary layered double hydroxides as high-performance bifunctional materials for oxygen electrocatalysis. Adv Energy Mater 5:1500245

[20] Sadighi Z, Liu J, Zhao L, Ciucci F, Kim J-K (2018) Metallic MoS_2 nanosheets: multifunctional electrocatalyst for the ORR, OER and Li-O_2 batteries. Nanoscale 10:22549–22559

[21] Li Y, Zhou Z, Yu G, Chen W, Chen Z (2010) CO catalytic oxidation on iron-embedded graphene: computational quest for low-cost nanocatalysts. J Phys Chem C 114:6250–6254

[22] Qiao B, Wang A, Yang X, Allard LF, Jiang Z, Cui Y (2011) Single-atom catalysis of CO oxidation using Pt1/FeOx. Nat Chem 3:634–641

[23] Yang X-F, Wang A, Qiao B, Li J, Liu J, Zhang T (2013) Single-atom catalysts: a new frontier in heterogeneous catalysis. Acc Chem Res 46:1740–1748

[24] Fei H, Dong J, Feng Y, Allen CS, Wan C, Volosskiy B (2018) General synthesis and definitive structural identification of MN_4C_4 single-atom catalysts with tunable electrocatalytic activities. Nat Catal 1:63–72

[25] Ling C, Bai X, Ouyang Y, Du A, Wang J (2018) Single molybdenum atom anchored on N-doped carbon as a promising electrocatalyst for nitrogen reduction into ammonia at ambient conditions. J Phys Chem C 122:16842–16847

[26] Wang SY, Yang ZX, Chu XL (2018) Design of efficient catalysts for Co oxidation on titanium carbide-supported platinum via computational study. J Phys Chem C 122:25974–25982

[27] Nie L, Mei D, Xiong H (2017) Activation of surface lattice oxygen in single-atom Pt/CeO_2 for low-temperature Co oxidation. Science 358:1419

[28] Lv X, Wei W, Sun Q, Li F, Huang B, Dai Y (2017) Two-dimensional germanium monochalcogenides for photocatalytic water splitting with high carrier mobility. Appl Catal B: Environ 217:275–284

[29] Wei Y, Ma Y, Wei W, Li M, Huang B, Dai Y (2018) Promising photocatalysts for water splitting in BeN_2 and MgN_2 monolayers. J Phys Chem C 122:8102–8108

[30] Seh ZW, Fredrickson KD, Anasori B, Kibsgaard J, Strickler AL, Lukatskaya MR, Gogotsi Y, Jaramillo TF, Vojvodic A (2016) Two-dimensional molybdenum carbide (MXene) as an efficient electrocatalyst for hydrogen evolution. ACS Energy Lett 1:589–594

[31] Gao G, O'Mullane AP, Du A (2017) 2D MXenes: A new family of promising catalysts for the hydrogen evolution reaction. ACS Catal 7:494–500

[32] Liu X, Wang P, Zhai H, Zhang Q, Huang B, Wang Z, Liu Y, Dai Y, Qin X (2018) Synthesis of synergetic phosphorus and cyano groups (C≡N) modified g-C_3N_4 for enhanced photocatalytic H_2 production and CO_2 reduction under visible light irradiation. Appl Catal B: Environ 232:521–530

[33] Li X, Dai Y, Li M, Wei W, Huang B (2015) Stable Si-based pentagonal monolayers: high carrier mobilities and applications in photocatalytic water splitting. J Mater Chem A 3:24055–24063

[34] Zhao P, Ma Y, Lv X, Li M, Huang B, Dai Y (2018) Two-dimensional III2-VI3 materials: promising photocatalysts for overall water splitting under infrared light spectrum. Nano Energy 51:533–538

[35] Wang S, He P, Jia L, He M, Zhang T, Dong F, Liu M, Liu H (2019) Nanocoral-like composite of nickel selenide nanoparticles anchored on two-dimensional multi-layered

graphitic carbon nitride: A highly efficient electrocatalyst for oxygen evolution reaction. Appl Catal B: Environ 243:463–469

[36] Zhou YN, Gao GP, Li Y, Chu W, Wang LW (2019) Transition-metal single atoms in nitrogen-doped graphenes as efficient active centers for water splitting: a theoretical study. Phys Chem Chem Phys 21:3024–3032

[37] Zhou YN, Gao GP, Kang J, Chu W, Wang LW (2019) Transition metal-embedded two-dimensional C_3N as a highly active electrocatalyst for oxygen evolution and reduction reactions. J Mater Chem A 7:12050

[38] Gao XP, Zhou YN, Tan YJ, Yang BW, Cheng ZW (2019) Single Mo atoms supported on N-doped carbon with N/C edge-site for enhanced electrochemical hydrogen evolution. Int J Hydrogen Energy 44:14861–14868

[39] Gao XP, Zhou YN, Tan YJ, Yang BW, Cheng ZW, Shen ZM (2019) Mo isolated single atoms on S, N-codoped carbon as efficient catalyst for hydrogen evolution reaction: a theoretical evaluation. Appl Surf Sci 473:770–776

[40] Morales-García Á, Calle-Vallejo F, Illas F (2020) MXenes: New Horizons in Catalysis. ACS Catal 10:13487–13503

[41] Oschinski H, Morales-García Á, Illas F (2021) Interaction of first row transition metals with M_2C (M = Ti, Zr, Hf, V, Nb, Ta, Cr, Mo, and W) MXenes: a quest for single-atom catalysts. J Phys Chem C 125:2477–2484

[42] Wang H, Lee HW, Deng Y, Lu Z, Hsu PC, Liu Y, Lin D, Cui Y (2015) Bifunctional non-noble metal oxide nanoparticle electrocatalysts through lithium-induced conversion for overall water splitting. Nat Commun 6:7261

[43] Wu Y, Li G-D, Liu Y, Yang L, Lian X, Asefa T, Zou X (2016) Overall water splitting catalyzed efficiently by an ultrathin nanosheet-built, hollow Ni_3S_2-based electrocatalyst. Adv Funct Mater 26:4839–4847

[44] Xu H, Cheng D, Cao D, Zeng XC (2018) A universal principle for a rational design of single-atom electrocatalysts. Nat Catal 1:339–348

[45] Gao G, Bottle S, Du A (2018) Understanding the activity and selectivity of single atom catalysts for hydrogen and oxygen evolution via ab initial study. Catal Sci Technol 8:996–1001

[46] Zhou Y, Gao G, Kang J, Chu W, Wang L-W (2019) Computational screening of transition-metal single atom doped C_9N_4 monolayers as efficient electrocatalysts for water splitting. Nanoscale 11:18169–18175

[47] Wang B, Wu Q, Zhang Y, Ma L, Wang J (2019) Auxetic B_4N monolayer: a promising 2D material with in-plane negative poisson's ratio and large anisotropic mechanics. ACS Appl Mater Inter 11:33231–33237

[48] Zhong CY, Wu WK, Ding GG, Liu Y, Li DF (2019) Two-dimensional honeycomb borophene oxide: strong anisotropy and nodal loop transformation. Nanoscale 11:2468–2475

[49] Zhao XF, Yang XY, Singh D, Panda PK, Luo W, Li YX (2020) Strain-engineered metal-free h-B_2O monolayer as a mechanocatalyst for photocatalysis and improved hydrogen evolution reaction. J Phys Chem C 124:7884–7892

[50] Guo J, Tian B, Shu H (2020) Multidimensional B_4N materials as novel anode materials for lithium ion batteries. Phys Chem Chem Phys 22:19913–19922

[51] Hu JP, Zhong CY, Wu WK, Liu N (2020) 2D honeycomb borophene oxide: a promising anode material offering super high capacity for Li/Na-ion batteries. J Phys Condens Matter 32:065001

[52] Li HF, Hao YQ, Sun D, Zhou D, Liu GT, Wanga H (2019) Mechanical properties and superconductivity in two-dimensional B_2O under extreme strain. Phys Chem Chem Phys 21:25859

[53] Yan L, Liu PF, Li H (2020) Theoretical dissection of superconductivity in two-dimensional honeycomb borophene oxide B_2O crystal with a high stability. npj Comput Mater 6:94

[54] Kresse G, Furthmiller J (1996) Efficiency of ab-initio total energy calculations for metals and semiconductors using a plane-wave basis set. Comp Mater Sci 6:15–50

[55] Kresse G, Furthmiller J (1996) Efficient iterative schemes for ab Initiototal-energy calculations using a plane-wave basis set. Phys Rev B 54:11169–11186

[56] Blöchl PE (1994) Projector augmented-wave method. Phys Rev B 50:17953–17979

[57] Perdew JP, Chevary JA, Vosko SH (1992) Atoms, molecules, solids, and surfaces: applications of the generalized gradient approximation for exchange and correlation. Phys Rev B 46:6671–6687

[58] Kresse G, Hafner J (1994) Ab Initio Molecular-dynamics Simulation of the Liquid-metal-amorphous-semiconductor Transition in Germanium. Phys Rev B 49:14251

[59] Grimme S, Ehrlich S, Goerigk L (2011) Effect of the damping function in dispersion corrected density functional theory. J Comput Chem 32:1456–1465

[60] Grimme S, Antony J, Ehrlich S, Krieg HA (2010) consistent and accurate ab initio parametrization of density functional dispersion correction (DFT-D) for the 94 elements H-Pu. J Chem Phys 132:154104

[61] Togo A, Tanaka I (2015) First principles phonon calculations in materials science. Scr Mater 108:1–5

[62] Gonze X, Lee C (1997) Dynamical matrices, Born effective charges, dielectric permittivity tensors, and interatomic force constants from density-functional perturbation theory. Phys Rev B 55:10355

[63] Liang XY, Wu CML (2020) Metal-free two-dimensional phosphorus carbide as an efficient electrocatalyst for hydrogen evolution reaction comparable to platinum. Nano Energy 71:104603

[64] Mavrikakis M, Hammer B, Nørskov JK (1998) Effect of strain on the reactivity of metal surfaces. Phys Rev Lett 81:2819–2822

[65] Hammer B, Nørskov JK (2000) Theoretical surface science and catalysis-calculations and concepts. Adv Catal 45:71–129

[66] Kitchin JR, Norskov JK, Barteau MA, Chen JG (2004) Role of strain and ligand effects in the modification of the electronic and chemical properties of bimetallic surfaces. Phys Rev Lett 93:156801–156805

[67] Stamenkovic V, Mun BS, Mayrhofer KJ, Ross PN, Markovic NM, Rossmeisl J, Greeley J, Nørskov JK (2006) Changing the activity of electrocatalysts for oxygen reduction by tuning the surface electronic structure. Angew. Chem. Int Ed 118:2963–2967

[68] Calle-Vallejo F, Krabbe A, Garcia-Lastra JM (2017) How covalence breaks adsorption-energy scaling relations and solvation restores them. Chem Sci 8:124–130

[69] Nørskov JK, Bligaard T, Logadottir A, Kitchin JR, Chen JG, Pandelov S, Stimming U (2005) Trends in the exchange current for hydrogen evolution. Electrochem Soc 152:J23–J26

[70] de Groot MT, Koper MT (2008) Redox transitions of chromium, manganese, iron, cobalt and nickel protoporphyrins in aqueous solution. Phys Chem Chem Phys 10:1023–1031

[71] Ling CY, Shi L, Ouyang YX, Zeng XC, Wang JL (2017) Nanosheet supported single-metal atom bifunctional catalyst for overall water splitting. Nano Lett 17:5133–5139

[72] Man IC, Su HY, Calle-Vallejo F, Hansen HA, Inoglu NG, Kitchin J (2011) Universality in oxygen evolution electrocatalysis on oxide surfaces. ChemCatChem 3:1159–1165

[73] Greeley J, Stephens IE, Bondarenko AS, Johansson TP, Hansen HA, Jaramillo TF (2009) Alloys of platinum and early transition metals as oxygen reduction electrocatalysts. Nat Chem 1:552–556